Experimental and Numerical Study on Transient Elongational Viscosity for PP/LDPE Blends

Yasuhiko Otsuki,[1*] Yoko Fujii,[2] Hiroko Sasaki,[1] Panitha Phulkerd,[2] and Masayuki Yamaguchi[2*]

1) Packing and Industrial Materials Laboratory,
Prime Polymer Co., Ltd.,
3 Chigusa-Kaigan, Ichihara, Chiba 299-0108 JAPAN

2) School of Materials Science,
Japan Advanced Institute of Science and Technology
1-1 Asahidai, Nomi, Ishikawa 923-1292 JAPAN

Running Head: Elongational Viscosity of PP/LDPE

* Corresponding to
Yasuhiko Otsuki (Yasuhiko.Otsuki@primepolymer.co.jp)
Masayuki Yamaguchi (m_yama@jaist.ac.jp)

Abstract

The transient uniaxial elongational viscosity for binary blends composed of polypropylene (PP) and low-density polyethylene (LDPE) was evaluated. A strain hardening behavior is detected for the blends, although LDPE is a dispersed phase. This behavior is attributed to LDPE dispersion deformation; the LDPE forms rigid fibers because of strain hardening. Rheological properties are calculated numerically by the Phan–Thien Tanner model by assuming a symmetric geometry with a periodic structure. Based on the simulation, we propose an appropriate LDPE to modify the processability of PP, at which the strain hardening in the elongational viscosity is required.

Keywords: polypropylene / low-density polyethylene / elongational viscosity / numerical simulation / viscoelasticity

1. Introduction

Polymer blending is one of the most important technologies that supports the modern plastics industry and can improve product performance, such as mechanical and thermal properties. Rheological property modification is another target of polymer blending to enhance the processability at various processing operations. The ability to increase the melt elasticity of a linear polymer is in strong demand in the industry. Several methods have been proposed to provide strain hardening in elongational viscosity, which is an important elastic property [1-10]. Among them, the simple addition of commercially available low-density polyethylene (LDPE) to isotactic polypropylene (PP) should be noted for potential industrial application [10]. In a previous study in which PP/LDPE blends were used, LDPE showed a slightly lower shear viscosity than PP, and it was suggested that the deformed LDPE droplets that were dispersed in the molten PP become rigid because of LDPE strain hardening during uniaxial elongational flow. Consequently, the blend behaved like a composite with rigid fibers, and led to a rapid increase in the elongational viscosity owing to the excess stress generation of a matrix between the fibrous dispersions [11-13]. Therefore, the viscosity ratio of the components, i.e., PP and LDPE, should have an important effect on the elongational viscosity of the blend systems, although such an effect has not been

revealed yet. One of the main purposes of this work is to clarify the effect of viscosity ratio on the strain hardening behavior in the transient elongational viscosity for PP/LDPE blends. We also study the growth curves of elongational viscosity for PP/LDPE blends by numerical simulation based on the mechanism mentioned above. Because measurement data of elongational viscosity often contain experimental error, predicted results by the numerical simulation should be considered seriously. In terms of PP processability, we proposed an appropriate LDPE as a processing modifier based on the simulation.

To date, considerable theoretical work has been conducted on two-phase flow that consists of a matrix and dispersions in polymer blends. Most studies have focused on droplet deformation owing to hydrodynamic force, and droplet breakup and/or coalescence with a consideration of the viscosity ratio, interfacial tension, capillary number, and flow pattern [14-21]. The simulation results provided information on material design and appropriate processing conditions to prepare polymer blends with fine dispersed droplets. In recent years, these research activities have progressed understanding, such as the simulation of mechanical behaviors of individually dispersed droplets in a three-dimensional space [22] and an analysis of complicated three-dimensional droplet deformation [23]. However, numerical studies on the

51 relationship between the structure of multiphase fluids and melt viscoelasticity has not
52 been carried out extensively. In terms of elongational viscosity, several studies were
53 reported for a suspension system with rigid particles dispersed in a viscous fluid [24-26].
54 In these studies, flow simulations were performed for a suspension with a number of
55 randomly dispersed rigid particles, and the simulations agreed well with the
56 experimental data for planar elongational flow. If we consider the calculation cost and
57 practical use, however, the calculation of a microstructural unit with one or two particles
58 based on an assumption of the periodic existence of particles is preferred to predict the
59 viscoelastic properties of a whole system. When rigid particles are arranged periodically
60 under uniaxial elongational flow, however, they approach each other in the transversal
61 direction to the flow, which leads to an unrealistic calculated result. Therefore, it is
62 necessary to set rigid particles that are arranged randomly in the matrix. When particles
63 are not rigid, they show a large deformation; in contrast, such an unrealistic structure
64 will not occur even under a large deformation. Consequently, an approximation of the
65 initial periodic structure will be kept until the final stage of deformation, which suggests
66 that viscoelastic properties of a system that contains flexible particles can be predicted
67 by a periodic local model.

68 Here, we carried out experiments using immiscible PP/LDPE blends with

69 various viscosity ratios, in which LDPE particles were dispersed in the PP matrix. The
70 experimental results obtained were compared with numerical simulations, which were
71 performed by assuming a symmetric geometry with a periodic structure. The
72 Lagrangian finite-element method with moving boundaries was used for isothermal
73 creeping-flow simulation. The viscoelastic characteristics of the samples were described
74 by the Phan–Thien Tanner (PTT) model with multiple relaxation modes. The
75 contribution of interfacial tension was ignored because it is insignificant compared with
76 the remarkable strain hardening of LDPE.
77

78 **2. Experimental Procedure**

79 **2.1 Materials**

80 A propylene homopolymer (PP; Primepolymer, Tokyo, Japan) and three types
81 of low-density polyethylene (LDPE) with different shear viscosities were used. The PP
82 melt-mass flow rate was 3.0 g/10 min at 230 °C for 2.16 kg and those of the LDPE were
83 3.7 for LDPE-L, 1.6 for LDPE-M, and 0.3 g/10 min for LDPE-H at 190 °C for 2.16 kg.
84 LDPE-L and LDPE-M were produced by an autoclave reactor, whereas LDPE-H was
85 produced by a tubular reactor. One of the LDPE samples, LDPE-M, and PP were used
86 in our previous study [10].

The PP/LDPE blend samples (PP:LDPE = 70:30, weight ratio) were prepared by an internal batch mixer (Labo-Plastmill 10M100, Toyo Seiki Seisaku-sho, Tokyo, Japan), and by rotating the blades at 30 rpm at 190 °C for 3 min, in the presence of 5,000 ppm of thermal stabilizers, such as tris(2,4-di-tert-butylphenyl)phosphate (Irgafos168, Ciba, Bazel, Switzerland) and pentaerythritol tetrakis(3-(3,5-di-tert-butyl-4-hydroxyphenyl)propionate) (Irganox1010, Ciba). The blended samples were compressed into flat sheets at 190 °C for 5 min by using a compression-molding machine, and quenched in the cooling unit.

2.2 Measurements

A cone-and-plate rheometer (AR2000ex, TA Instruments, New Castle, DW) was used to evaluate the frequency dependence of the shear storage modulus *G'* and loss modulus *G"* at 190 °C. The cone angle was 4° and its diameter was 25 mm. The growth curves of the transient uniaxial elongational viscosity were measured by the rotational rheometer equipped with a universal testing platform (SER2-G, Xpansion Instruments, Tallmadge, OH) at 190 °C. Rectangular 10-mm-wide, 15-mm-long, and 0.8-mm-thick samples were used for the measurements.

3. Numerical Simulation

3.1 Governing equations

By considering the flow of a highly viscous fluid, ignoring the effects of inertia and gravity, and assuming that the fluid is isothermal and incompressible, the equation of motion and the equation of continuity were given by equations (1) and (2), respectively.

$$-\nabla p + \nabla \cdot \boldsymbol{\tau} = \mathbf{0} \tag{1}$$

$$\nabla \cdot \mathbf{v} = \mathbf{0} \tag{2}$$

where p is the isotropic pressure, $\boldsymbol{\tau}$ is the stress tensor, and $\mathbf{v}$ is the velocity vector.

As the viscoelastic constitutive equation, the PTT model with a multiple relaxation mode [27] represented by equations (3), (4), and (5) was used, in which the stress-coefficient function $\mathrm{Y}_i(\boldsymbol{\tau}_i)$ was expressed by the exponential form;

$$\mathrm{Y}_i\left(\boldsymbol{\tau}_i\right)\boldsymbol{\tau}_i + \lambda_i\left[\frac{\xi}{2}\overset{\triangle}{\boldsymbol{\tau}_i} + \left(1-\frac{\xi}{2}\right)\overset{\triangledown}{\boldsymbol{\tau}_i}\right] = 2\eta_{0i}\mathbf{D} \tag{3}$$

$$\mathrm{Y}_i\left(\boldsymbol{\tau}_i\right) = \exp\left(\frac{\zeta}{G_i}\mathrm{tr}\left(\boldsymbol{\tau}_i\right)\right) \tag{4}$$

$$\boldsymbol{\tau} = \sum_{i=1}^{n}\boldsymbol{\tau}_i \tag{5}$$

where $\mathbf{D}$ is the deformation velocity tensor. $\boldsymbol{\tau}_i$, λ_i, η_{0i},, and G_i are the stress tensor, relaxation time, zero shear viscosity, and relaxation modulus of the mode i, respectively.

122 The superscript $\triangle$ and ∇ represent the lower- and upper-convected time derivatives,
123 respectively, and ζ and ξ are the non-linear parameters used in the PTT model.
124
125 **3.2 Numerical procedure**
126 We reported previously flow analysis during the stretching of foam with a
127 moving boundary based on the Galerkin finite-element method [28]. In this study, the
128 program was expanded to incorporate the dispersed phase as a viscoelastic fluid for the
129 flow analysis. A Lagrange mesh was used, in which the positions of the nodes follow
130 the mass point with the flow in the matrix and dispersed phases. The method to
131 calculate the flow field at time step $n + 1$ based on that at time step n was as follows. If
132 we assume that the coordinate value of a certain node is **X** and the velocity vector is **v**,
133 the coordinate value of the node at step $n + 1$ was determined by the central difference
134 method given by equation (6).
135 $$\mathbf{X}_{n+1} = \mathbf{X}_n + \frac{\mathbf{v}_{n+1} + \mathbf{v}_n}{2} \Delta t \quad (6)$$
136 where subscripts n and $n + 1$ indicate the values at the n and $n + 1$ steps, respectively,
137 and Δt is the time between consecutive steps.
138 To calculate the velocity field, a mesh that was composed of each node of $n + 1$
139 steps was used to calculate equation (7) by the Galerkin FEM;

$$-\nabla p + 2\eta_r \nabla \cdot \mathbf{D}_{new} = -\nabla \cdot \boldsymbol{\tau} + 2\eta_r \nabla \cdot \mathbf{D}_{old} \quad (7)$$

where the reference viscosity η_r was a calculation parameter that can be set arbitrarily. η_r was determined by the stress and velocity of the field [29]. The subscripts *old* and *new* represent the known and unknown values, respectively. In the iterative calculation, $\boldsymbol{\tau}$ and $\mathbf{D}$ on the right of equation (7) substituted the values obtained in the previous calculation, and the procedure to calculate new values of unknown variables on the left side was repeated. In this analysis, a decoupled method was used, in which stress and velocity were solved separately and substituted alternately. Square elements with nine velocity nodes and four pressure nodes were used. To calculate the viscoelastic stress, a short time step was set according to the relaxation time, and the constitutive equation was integrated by the Runge–Kutta method with the stress of n steps as an initial value, and the stress value at the $n + 1$ step was obtained.

At this multiphase flow analysis, we assumed no slippage at the interface. Therefore, the velocity is continuous at the interface, although other physical quantities, such as the velocity gradient, stress, and pressure, are discontinuous. For this reason, double nodes were arranged at the interface, in which different values of the physical quantities were used [30]. For the velocity analysis, however, the same nodes were shared for the matrix and dispersed phases to maintain the surface-force continuity. As

158 described above, the prediction and correction of the velocity, the coordinates of the
159 nodal point, and the stress were repeated until the calculated value converged, and then
160 the process shifted to the next step (time).

161

162 **3.3 Analytical model**

163 By assuming a simplified initial structure shown in Figure 1, the
164 two-dimensional flow analysis was performed under uniaxial elongational flow of
165 two-phase materials. A local part was cut because of the periodicity and symmetry. Then
166 the unit cell in Figure 1 was analyzed. By assuming a fine-grained hexagonal lattice of
167 the dispersed phase as the initial morphology, a vertical rectangular model was set.

168

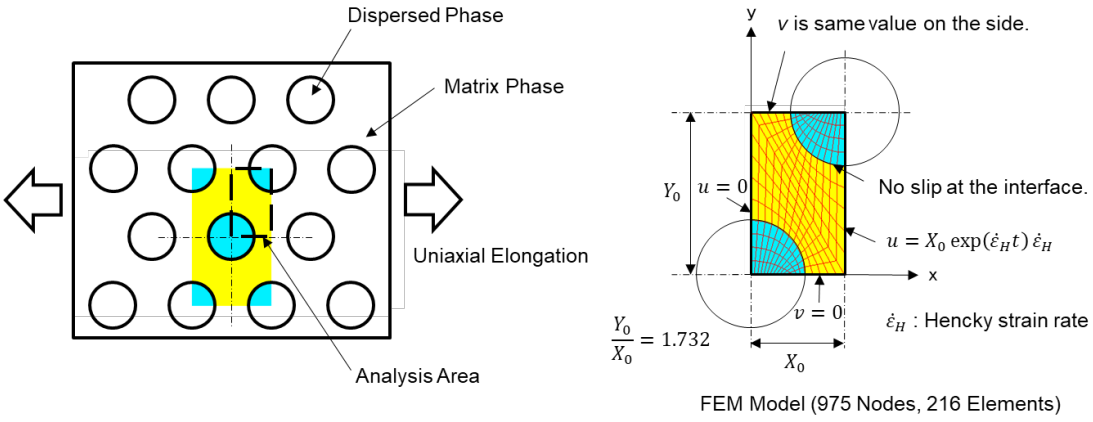

169

170 **Figure 1.** Simplified two-dimensional model of two-phase elongational flow.

171

Figure 1 represents the model with 30% of the dispersed phase. In the model with 15% dispersed phase, the radius is reduced further in accordance with the volume fraction. This model allows dimensionless analysis; i.e., the absolute value of the domain size does not affect the analysis result because the surface tension is not considered. Here, a velocity boundary condition with a fixed amount was set in the x direction only at the right side of the analysis region, and the velocities in the direction perpendicular to the boundary plane along the x and y axes were set to zero. Because the x direction velocity at the right side of the analysis area was set, the Hencky strain rate $\dot{\varepsilon}_H$ of the field was a constant. As a result, the boundary moved with an exponential function. A two-dimensional flow analysis was performed by assuming that the physical quantities were constants in the depth direction z, and a compression strain rate of $\dot{\varepsilon}_H / 2$ was set uniformly in the z direction. Therefore, the field deformation became uniaxial elongation. At the boundary of the upper side of the analysis area, the velocity in the y direction was set to be unknown but the values were the same in this plane. Because incompressibility was assumed, the velocity was calculated (the elongational strain rate in the y direction was $-\dot{\varepsilon}_H / 2$). For the FEM model, as shown in the figure on the right (Figure 1), a mesh with 975 nodes and 216 elements was constructed. As for the time step in unsteady analysis, the time until the Hencky strain reached six was divided into

3000 steps for each elongational strain rate. A calculation of the elongational viscosity was obtained by dividing the average value of the normal stress difference in the *y* direction by the elongational strain rate. The inhomogeneity in the *x* direction was considered and the elongational viscosity was calculated by dividing the average value of the normal stress differences across the whole analysis region by the elongational strain rate. As a test analysis of the FEM simulation, the elongational viscosity was calculated by setting the same viscoelastic characteristics for the matrix and dispersed phases, and this viscosity was compared with the elongational viscosity of the single material that was calculated directly from the constitutive equation. We confirmed that both methods gave the same results, which shows that the simulation method is reliable.

4. Results and Discussion

4.1 Rheological properties of pure polymers

Figure 2 shows the oscillatory shear moduli, such as the storage modulus *G'* and loss modulus *G"*, as a function of angular frequency ω for the pure samples at 190 °C. As shown in the figure, the oscillatory moduli of LDPE-H are higher than those of PP, whereas LDPE-L has lower moduli. The loss moduli of LDPE-M are slightly lower than those of PP. The relaxation spectra that were used for the simulation are estimated

208 from the experimental data, as shown by the solid (*G'*) and dotted (*G"*) lines.

209

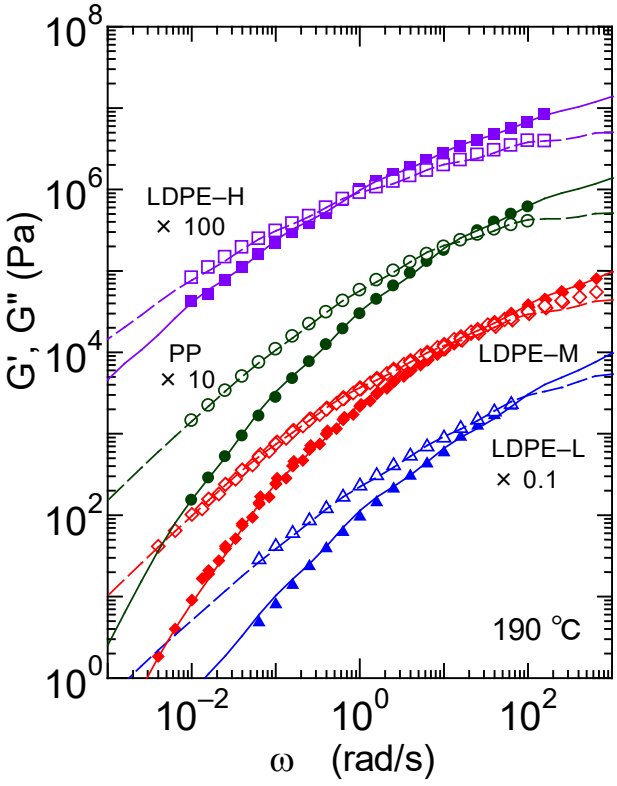

210

211 **Figure 2.** Experimental (symbols) and calculated (lines) results of the frequency
212 dependence of shear storage modulus *G'* (closed symbols and solid lines) and loss
213 modulus *G"* (open symbols and dotted lines) for PP (circles), LDPE-L (triangles),
214 LDPE-M (diamonds), and LDPE-H (squares) at 190 °C. The vertical axes were shifted.

215

216 Transient elongational viscosities for PP, LDPE-L, and LDPE-H are shown in
217 Figure 3. The data for LDPE-M were shown elsewhere [10]. The strain hardening
218 behavior is detected as a steep slope for LDPE-L, and is similar to LDPE-M. In contrast,

LDPE-H shows weak strain hardening, i.e., a gentle slope, which is presumed to be attributed to the difference in the branch structure. Because LDPE-H is produced in a tubular reactor, the long-chain branch structure is not well-developed compared with the other LDPE samples that were produced by an autoclave reactor [31-33]. The elongational viscosities of LDPE-L are lower than those of the pure PP at the beginning of the elongational flow (short time/strain region) and increase rapidly with time/strain. Finally, they exceed the values of the pure PP owing to the strain hardening. For LDPE-H, the elongational viscosities are higher than those of the pure PP from the beginning of the stretching.

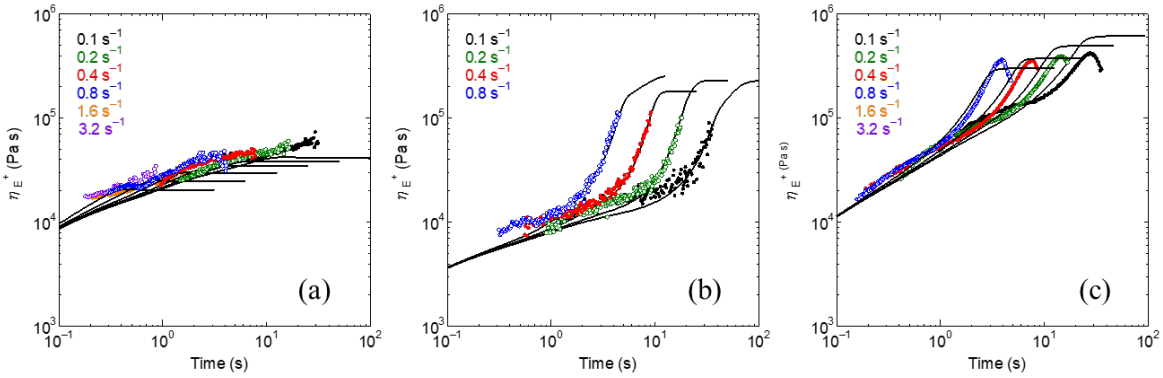

Figure 3. Transient elongational viscosity with time at various Hencky strain rates at 190 °C for (a) PP, (b) LDPE-L, and (c) LDPE-H. The experimental data are shown as circles and the solid lines represent the calculated values.

234 The calculated values using the Runge–Kutta method that are derived directly
235 from the PTT constitutive equation are also shown in Figure 3 by the solid lines. It is
236 found that the experimental data can be predicted successfully. The non-linear
237 viscoelastic parameters used in the simulations, such as ξ and ζ, are summarized in
238 Table 1 with the relaxation spectra calculated from linear viscoelasticity.

239

240 Table 1 Relaxation spectra and PTT model parameters.

λ (s)	G (Pa)			
	PP	LDPE-L	LDPE-M	LDPE-H
0.001	90000	100000	80000	90000
0.01	62000	38000	40000	53000
0.1	26000	8600	14000	26000
1	4800	1800	3600	11500
10	520	150	400	3200
100	20	10	8	600
1000	-	-	-	80
PTT Model Parameters				
ξ	0.12	0.15	0.15	0.15
ζ	0.5	0.005	0.005	0.08

241

242 **4.2 Uniaxial elongational viscosity of blends**

243 As reported previously [10], PP/LDPE-M (70/30) and (85/15) showed a
244 marked strain hardening behavior with an intense fashion of PP/LDPE-M (70/30). The
245 calculated transient elongational viscosities η_E^+ are compared with the experimental
246 data in Figure 4 with other blends that contain low-viscosity LDPE-L and high-viscosity

LDPE-H. The contributions of PP and LDPE to the elongational viscosity, calculated from the stress distribution generated in the two materials, are also indicated in the figure. First, both blend samples, i.e., PP/LDPE-L (70/30) and PP/LDPE-H (70/30), show a clear strain hardening behavior, which is similar to the PP/LDPE-M blends. Second, it was confirmed that the calculation predicts the results.

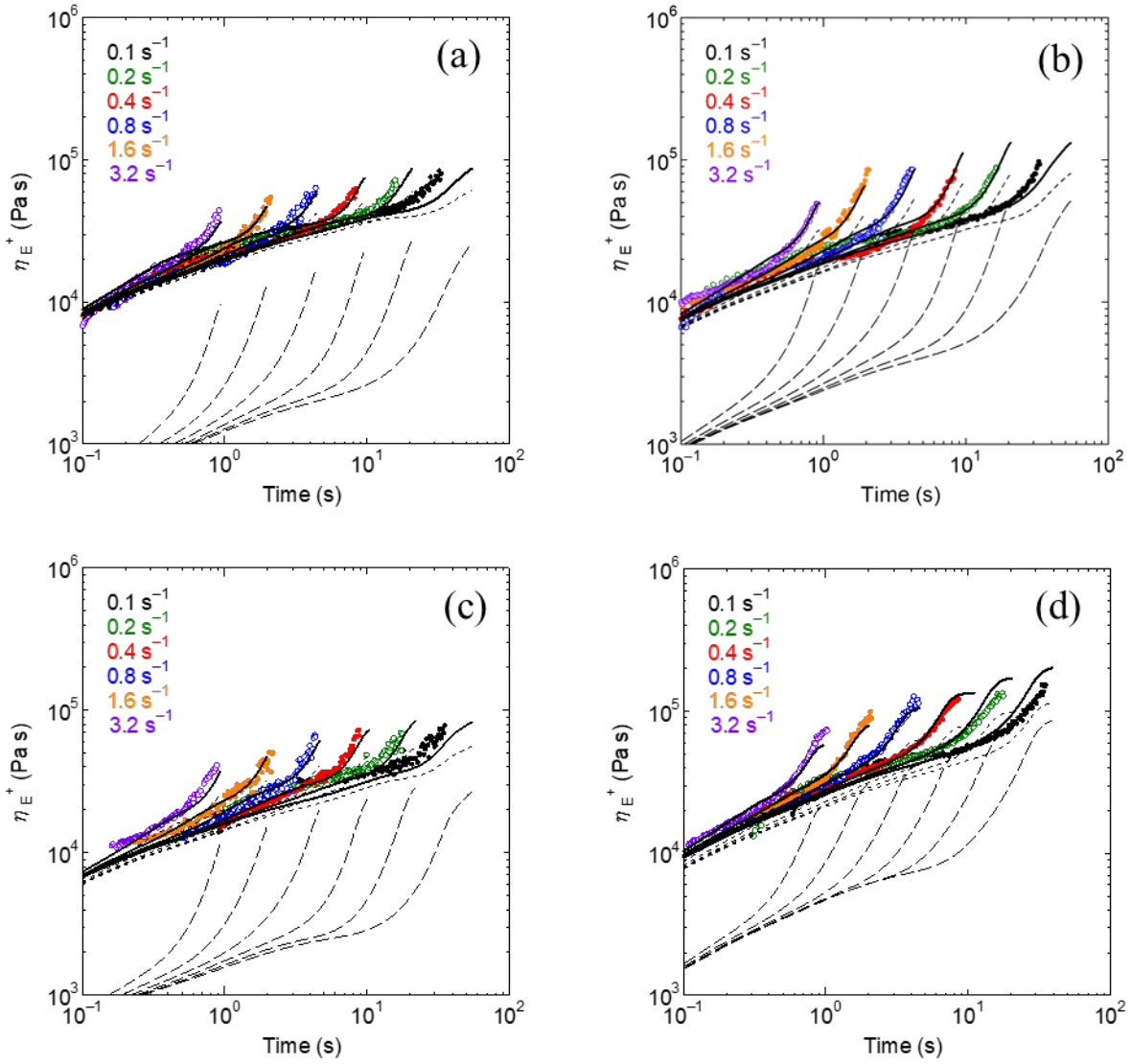

Figure 4. Transient elongational viscosity η_E^+ with time at various Hencky strain rates at 190 °C for (a) PP/LDPE-M (85/15), (b) PP/LDPE-M (70/30), (c) PP/LDPE-L (70/30), and (d) PP/LDPE-H (70/30). The solid lines represent the numerical results. The contributions of the stress generated in PP (dotted lines) and LDPE (dashed lines) are also indicated.

When uniaxial elongational flow is applied to a blend having sea-island structure with soft dispersion, the spherical dispersed droplets are elongated to the flow direction and turns into prolonged shape. Then, the interaction between dispersed droplets must be taken into consideration eventually. If this situation is strictly and numerically analyzed using a single domain, the two-dimensional axisymmetric problem occurs, and therefore, a three-dimensional analysis is required. In the present study, however, this phenomenon is approximated by describing in a 2D rectangular coordinate system having sheet-like or ribbon-like dispersed (2D) droplets. Although the error caused by this approximation will be evaluated in near future as compared with the exact 3D model, it is expected that similar results are obtained by both models for the deformation mode and the growth of stress balance around the dispersed droplets. In fact, it was confirmed that the calculation of the approximated model successfully

predicts the experimental data of the uniaxial elongational viscosities as shown in Figure 4, suggesting that this model is practically effective.

Here, the transient elongational viscosity of the blend material is estimated by a simple mixing rule and compared with the calculation result of the FEM analysis. Assuming the affine deformation of the dispersed phase, the transient viscosity of the mixture can be estimated by the following simple equation;

$$\eta_E^+\left(t,\dot{\varepsilon}_H\right)=\phi_c\eta_{cE}^+\left(t,\dot{\varepsilon}_H\right)+\phi_d\eta_{dE}^+\left(t,\dot{\varepsilon}_H\right) \quad (8)$$

where η_E^+, η_{cE}^+, and η_{dE}^+ are the elongational viscosities of the mixture, continuous phase, and dispersed phase, and ϕ_c and ϕ_d are the volume fractions of the continuous and dispersed phases, respectively.

The elongational viscosity of the mixture was estimated by equation (8) using the calculated elongational viscosities of the single materials. As shown in Figure 5, it was found that similar results to the FEM calculation were obtained for PP/LDPE-M, suggesting that the simple mixing rule is effective when the constituent materials show similar viscosities. However, differences appear for the other blends. When the dispersed phase has lower viscosity, i.e., PP/LDPE-L, the strain hardening occurs earlier for the FEM simulation. For the blend system, the internal strain of the dispersed droplets develops more quickly than the external strain, as will be mentioned later with

290 the discussion on structure change. In the case that the dispersed phase has higher
291 viscosity, i.e., PP/LDPE-H, in contrast, the deformation of the dispersed droplets does
292 not catch up with the external strain. Consequently, the strain hardening occurs at a
293 longer time (larger strain) than the result by the simple mixing rule. Furthermore, the
294 viscosity levels in the strain hardening region are considerably lower than those by the
295 simple mixing rule. This is attributed to the low aspect ratio of dispersed LDPE-H.
296 Batchelor [11] and Mewis and Metzner [12] clarified that the enhancement of
297 elongational viscosity by fiber addition is pronounced with an increase in fiber aspect
298 ratio.
299

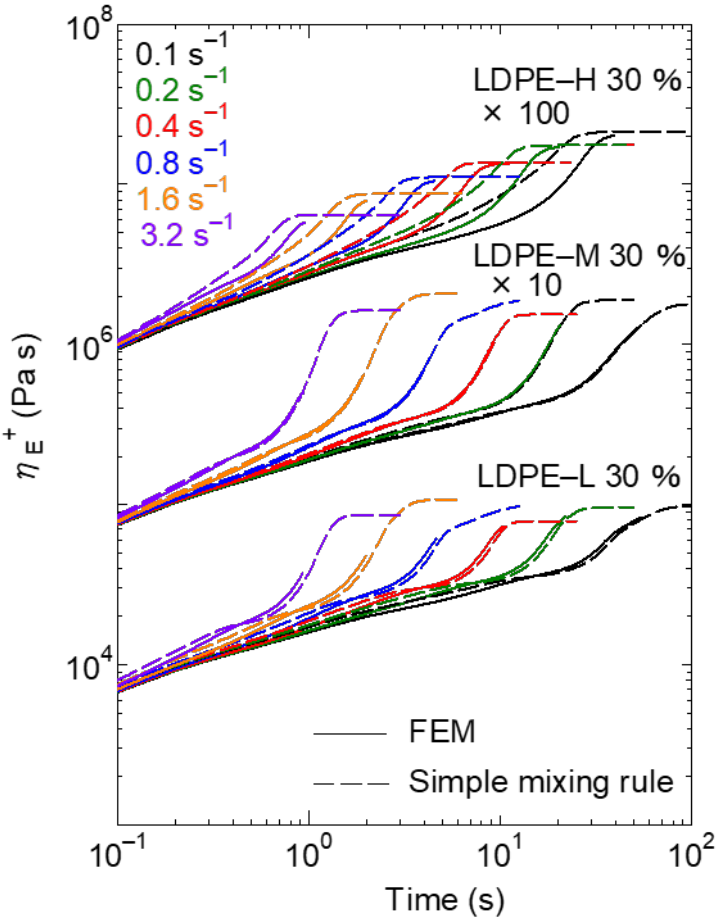

300

301 **Figure 5.** Comparison of elongational viscosities predicted by the finite element method

302 (solid lines) and by the simple mixing rule (dashed lines).

303

304 The contribution of the continuous phase to the elongational viscosity for the

305 blends increases in the final stage in each system as shown in Figure 4. This indicates

306 that there is indeed an effect of non-affine deformation of the continuous phase, i.e.

307 higher elongation strain rate and/or higher normal stress difference in some area. Figure

308 4 also indicates that the contribution of the dispersed phase increases rapidly in the large

309 deformation area, suggesting that the dispersed phase eventually shows pseudo affine
310 deformation.

311 To clarify the difference in the strain hardening for the blend samples
312 quantitatively, the calculated values of the blends with 30% LDPE are shown in Figure
313 6 with those of the pure components, i.e., PP and LDPE. As compared with the
314 PP/LDPE-H, both PP/LDPE-M and PP/LDPE-L show strain hardening in the long time
315 (large strain) region; i.e., the strain hardening is delayed. This is reasonable because a
316 large strain is required for LDPE-L and LDPE-M to show a higher elongational
317 viscosity than PP, although the difference in onset of strain hardening between
318 PP/LDPE-M and PP/LDPE-L is minimal, and will be discussed later. In contrast, strain
319 hardening occurs in the short time region for the blend with LDPE-H. This is owing to
320 the prompt stress growth of LDPE-H. Even though strain hardening of the dispersed
321 droplets in PP/LDPE-H is delayed from that of LDPE-H alone, the strain hardening still
322 occurs in the shorter time region as compared with the other blends.
323

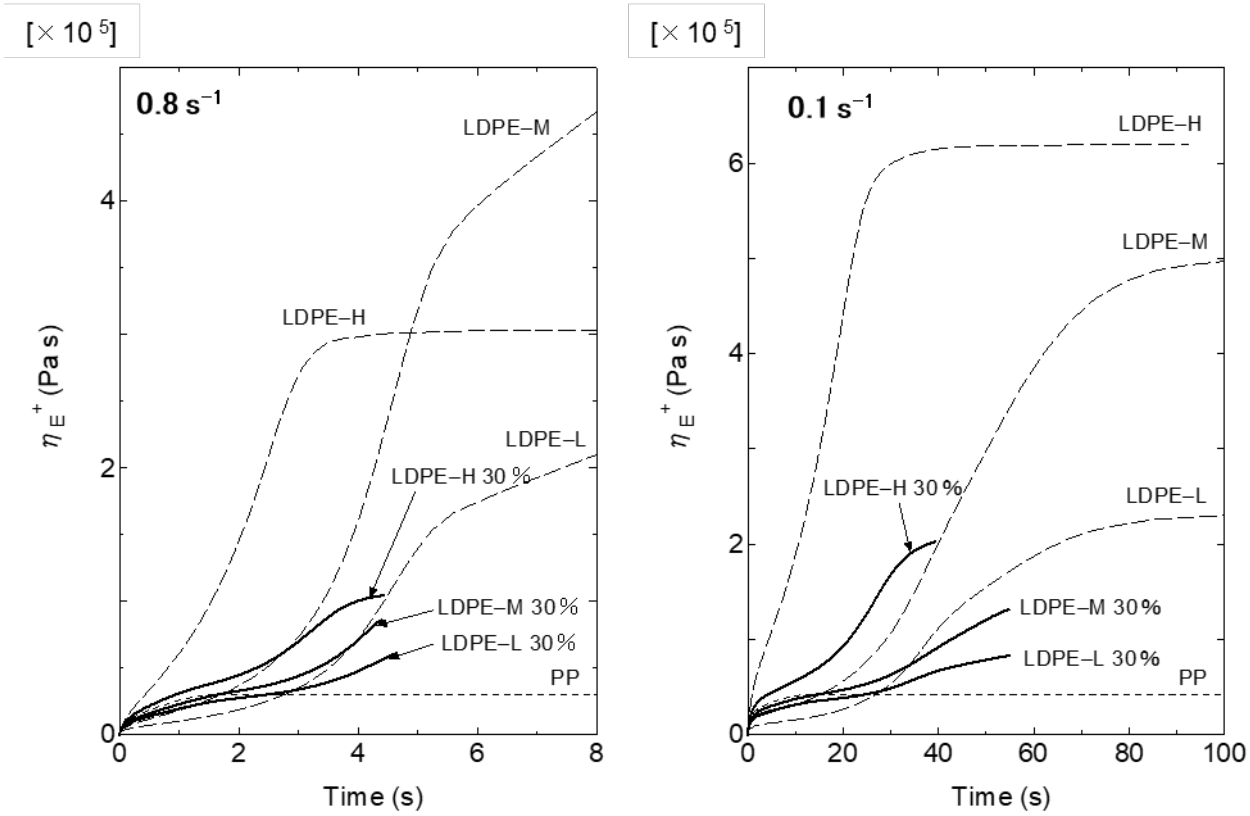

Figure 6. Calculated elongational viscosity of PP, LDPE, and the blend with 30% LDPE. (Left) $\dot{\varepsilon}_H = 0.8$ s^{-1} and (right) $\dot{\varepsilon}_H = 0.1$ s^{-1}.

4.3 Development of morphology and stress distribution

As commented previously, the shape of the dispersed phase has a strong impact on the rheological behavior under elongational flow. Therefore, the structure development of the blends containing 30% of LDPE is calculated. Figure 7 shows the structures during stretching at Hencky strains ε_H of 1.2 and 2.4.

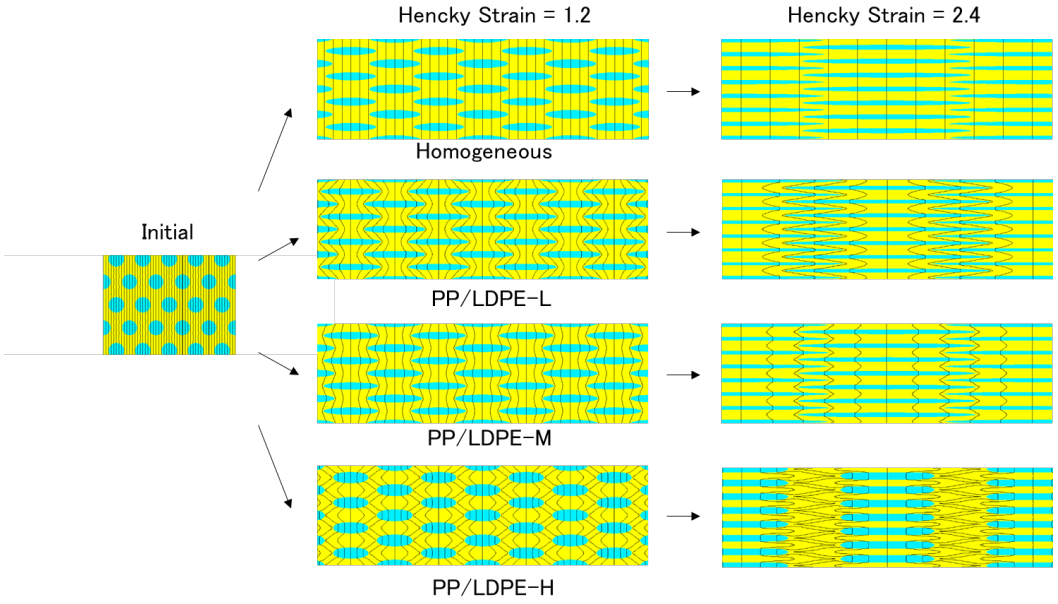

334

335 **Figure 7.** Numerical results of structure development under uniaxial elongational flow

336 for blends with 30% LDPE.

337

338 In the figure, longitudinal lines at the initial state are inserted periodically to

339 comprehend the deformation easily. Furthermore, the structures are magnified to see the

340 lines clearly at Hencky strains of 1.2 and 2.4. For the homogeneous material, in which

341 continuous and dispersed phases are the same substance, both phases deform in the

342 same way. Therefore, the lines remain straight with an increase in the distance as the

343 deformation progresses. When the dispersed phase shows a different viscoelasticity

344 from the continuous phase, the lines become distorted. For PP/LDPE-L, the dispersions

345 deform more rapidly than the external deformation in the early stage of elongation,

346 which leads to prolonged droplets promptly. Such a structure development of blends

with a sea-island morphology has been reported previously by advanced research groups [15,19,34]. Similarly, the LDPE-M dispersions, which show a slightly lower viscosity than the continuous PP in the short time region, deform more than the external strain, although their deformation is smaller than that of the LDPE-L. Because LDPE-L shows a larger deformation in the blend, the onset strain to show strain hardening is not so different from that for PP/LDPE-M (Figure 6). In contrast, the LDPE-H deformation is delayed because of their higher viscosity than the continuous PP. Because the deformation of the dispersed phase cannot catch up with the continuous one for PP/LDPE-H, the LDPE-H droplets do not overlap each other even under a large deformation, and thus nonuniformity appears in the width direction. In this analysis model, periodic configuration is assumed, and the dispersed droplets are arranged straight vertically. Since the dispersed phase is not so hard for PP/LDPE-H, the elongational viscosity could be predicted by averaging the stress in the width direction. However, if the viscosity of a dispersed phase is too high to be undeformable during elongational flow; i.e., dispersed particles behave as rigid body like inorganic fillers, this analytical model will not be applicable.

Figure 8 shows the ratio of Hencky strain rate of a dispersion $\dot{\varepsilon}_{Hd}$ to the external strain rate $\dot{\varepsilon}_H$, i.e., $\dot{\varepsilon}_{Hd} / \dot{\varepsilon}_H$, as a function of the external strain for the blends

365 with 30% LDPE. The strain rate of a dispersion is determined by (dR_1/dt) / R_1, where R_1
366 is the major radius of the dispersion.
367

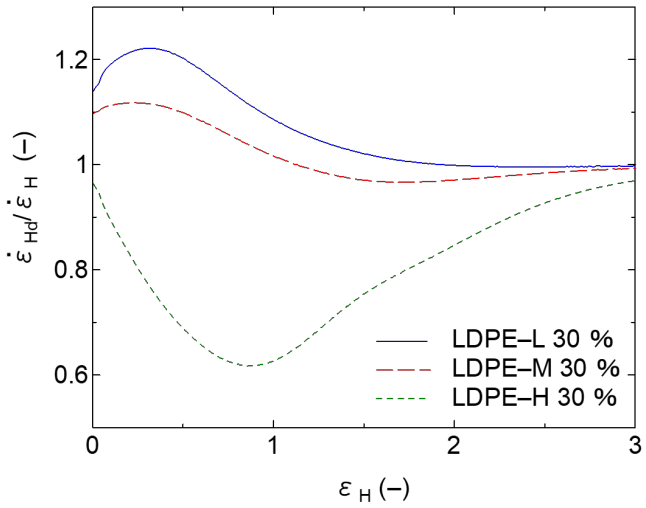

368

369 **Figure 8.** Ratio of the Hencky strain rate of the dispersion to the external strain rate,
370 $\dot{\varepsilon}_{Hd} / \dot{\varepsilon}_H$, as a function of the external strain ε_H for PP/LDPE (70/30) at $\dot{\varepsilon}_H = 0.8$ s^{-1}.
371

372 Figure 8 shows that the effect of the LDPE species appears in the early stage of
373 the elongational flow. Furthermore, the direction of the deviation, i.e., upper (larger than
374 unity) or lower (smaller than unity), is determined by the viscosity ratio of PP to LDPE.
375 It is interesting to note that the ratio of the blend with LDPE-M is larger than unity
376 initially, and smaller than unity beyond a strain of 1.1; i.e., the dispersions act as long
377 rigid fibers.

378 It is also found that the ratios of the strain rates, i.e., $\dot{\varepsilon}_{Hd} / \dot{\varepsilon}_H$, gradually

379 approaches one for all blends, although the values at the initial stage are determined by
380 the viscosity ratio of PP to LDPE. This result indicates that all systems are approaching
381 affine deformation under the large deformation, which is prominent especially for the
382 blend systems with LDPE-L and LDPE-M. Therefore, the values predicted by the
383 simple mixing rule were closed to those of the FEM analysis as shown in Figure 5.

384 Figure 9 shows the distributions of shear stress τ_{xy} at the boundary surface of a
385 dispersion and tensile stress τ_{xx} - τ_{yy} at the center of a dispersion in the *x* direction during
386 stretching at $\dot{\varepsilon}_H = 0.8$ s^{-1} for PP/LDPE-M (70/30). The shear stress shows the
387 maximum at the end of the elliptical dispersion, and decreases toward the center, which
388 balances the tensile stress that is generated in the dispersion. With an increase in the
389 aspect ratio of the dispersion, the shear stress, especially near the end parts of the
390 dispersion, is enhanced significantly. Moreover, the elongational stress in the dispersion
391 is high as revealed by the previous researches [35,36]. As a result, the apparent
392 elongational viscosity for the whole system is enhanced. Such a stress distribution was
393 also confirmed in the elastic deformation analysis for a composite material with long
394 cylindrical fibers [37,38]. In the present system, however, a large elongational stress is
395 detected for the whole of the LDPE dispersion, which is different from the stress
396 distribution in the cylindrical fiber composite. This phenomenon occurs because the

397 cross-sectional area of the dispersion decreases toward the end, which leads to a high
398 elongational stress near the end [39].
399

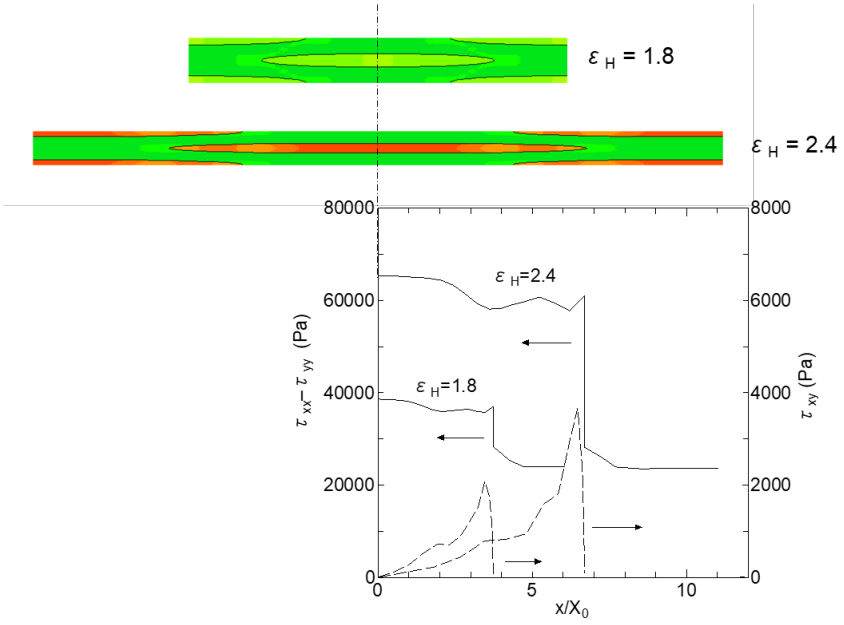

400
401 **Figure 9** Distributions of tensile stress at the center of the dispersed phase and shear
402 stress at the surface of the dispersed phase at ε_H =1.8 and 2.4 during elongation flow at
403 $\dot{\varepsilon}_H$ = 0.8 s^{-1} for PP/LDPE-M (70/30).
404
405 It is found that the elongation stress acting on the dispersed phase is
406 considerably higher than the shear stress at the surface of the dispersion. When the
407 aspect ratio increases, the interfacial area of the dispersed droplets increases greatly
408 with the decrease in the vertical cross-sectional area. As a result, dispersed droplets with
409 high viscosity can be deformed affinely. Figure 9 also shows that the shear stress is low

near the center of the dispersed droplet. A similar situation was detected also for a composite system with long fibers, suggesting that the center area is affinely deformed. Although the strain hardening occurs in the dispersion under a large strain, the dispersion shows pseudo affine deformation following the external strain rate. Thus, high elongational stress is developed in the dispersed phase, which directly contributes to the increase in the elongational viscosity of the blend. This situation is magnified with increase in the volume fraction of the dispersed phase.

The simulation result indicates that the elongational viscosity of the PP/LDPE blend systems can be controlled by the ratio of the elongational viscosities between PP and LDPE and the strain hardening behavior of LDPE. When the LDPE shows a lower viscosity, it turns into a fibrous shape promptly. Then, a steep increase in elongational viscosity, i.e., pronounced strain hardening, is provided for the blend after stretching to some degree; i.e., the strain hardening is delayed. When the strain hardening is required in the early stage of flow, e.g., reduction of neck-in level at T-die extrusion, LDPE that has a slightly higher shear viscosity with a marked strain hardening in the elongational viscosity is recommended. In the case of foaming, LDPE with a low shear viscosity would be recommended to show a large expansion ratio because the strain hardening

428 occurs at a large strain.

429

430 **5. Conclusions**

431 The effect of LDPE addition on the rheological properties of PP under uniaxial
432 elongational flow is investigated. The LDPE addition is found to provide strain
433 hardening in the transient elongational viscosity for PP although LDPE is the dispersed
434 phase. Moreover, the experimental results were predicted by the numerical simulation
435 by using the PTT model with multiple relaxation modes by assuming the symmetric
436 geometry with a periodic structure. The transient elongational viscosity for pure LDPE
437 determines the critical strain to show strain hardening and the magnitude of strain
438 hardening for the blends. When the shear viscosity of LDPE is lower than that of PP, the
439 strain hardening appears later with a steep slope, where LDPE dispersions have a high
440 aspect ratio. In contrast, the blend with LDPE with a higher viscosity shows strain
441 hardening in the early stage of the flow. These results obtained in this study will be
442 useful to select an appropriate LDPE as a processing modifier for PP in real processing
443 operations.

444

445 **References**

1. Yamaguchi, M.; Miyata, H. *Polym. J*. **2000**, *32*, 164-170.
2. Sugimoto, M.; Masubuchi, T.; Takimoto, J.; Koyama, K. *Macromolecules* **2001**, *34*, 6056-6063.
3. Kurose, T.; Takahashi, T.; Sugimoto, M.; Taniguchi, T.; Koyama, K. *Nihon Reoroji Gakkaishi*, **2005**, *33*, 173-182.
4. Yamaguchi, M.; Wakabayashi, T. *Adv. Polym. Technol.* **2006**, *25*, 236-241.
5. Mieda, N.; Yamaguchi, M. *J. Non-Newtonian Fluid Mech.* **2011**, *166*, 231-240.
6. Yokohara, T.; Nobukawa, S.; Yamaguchi, M. *J. Rheology* **2011**, *55*, 1205-1218.
7. Yamaguchi, M.; Yokohara, T.; Ali, M. A. B. *Nihon Reoroji Gakkaishi*, **2013**, *41*, 129-135.
8. Siriprumpoonthum, M.; Nobukawa, S.; Satoh, Y.; Sasaki, H.; Yamaguchi, M. *J. Rheology* **2014**, *58*, 449-466.
9. Seemork, J.; Sako, T.; Ali, M. A. B.; Yamaguchi, M. *J. Rheology* **2017**, *61*, 1-11.
10. Fujii, Y.; Nishikawa, R.; Phulkerd, P.; Yamaguchi, M. *J. Rheology* **2019**, 63, 11-18.
11. Batchelor, G. K. *J. Fluid Mech.* **1971**, *46*, 813-829 (1971).
12. Mewis, J.; Metzner, A. B. *J. Fluid Mech.* **1974**, *62*, 593-600.
13. Laun, H. M. *Colloid Polym. Sci*. **1984**, *262*, 257-269.
14. Toose, E. M.; van Damme, R. M. J.; van den Ende, H. T. M.; Geurts, B. J.; Kuerten, J. M. G. *J. Non-Newtonian Fluid Mech*. **1995**, *60*, 129–154.

15. Delaby, I. Ernst, B.; Froelich, D.; Muller, R. *Polym. Eng. Sci*. **1996**, *36*, 1627-1635.

16. Ramaswamy, S.; Leal, L. G. *J. Non-Newtonian Fluid Mech.* **1999**, *85*, 127–163.

17. Ramaswamy, S.; Leal, L.G. *J. Non-Newtonian Fluid Mech.* **1999**, *88*, 149–172.

18. Hooper, R. W.; de Almeida, V. F.; Macosko, C. W.; Derby, J. J. *J. Non-Newtonian Fluid Mech.* **2001**, *98*, 141–168.

19. Cristini, V.; Hooper, R. W.; Macosko, C. W.; Simeone, M.; Guido, S. *Ind. Eng. Chem. Res.* **2002,** *41,* 6305-6311

20. Mukherjee, S.; Sarkar, K. *J. Non-Newtonian Fluid Mech.* **2009**, *160*, 104–112.

21. Cardinaels, R.; Afkhami, S.; Renardy, Y.; Moldenaers, P. *J. Non-Newtonian Fluid Mech.* **2011**, *166*, 52–62.

22. Skartilien, R.; Sollum, E.; Akselsen, A. Meakin, P. *Rheol. Acta* **2002**, *51*, 649-673.

23. Isbassarov, D.; Rosti, M. E.; Ardekani, M. N.; Sarabian, M.; Hormozi, L. B.; Tammisola, O. *Int. J. Numerical Methods Fluids* **2018**, *88*, 521-543.

24. Hwang, W. R.; Hulsen, M. *J. Non-Newtonian Fluid Mech.* **2006**, *136*, 167-178.

25. D'Avino, G.; Maffettone, P. L.; Hulsen, M. A.; Peters, G. W. M. *J. Comp. Phys.* **2007**, *226*, 688-711.

26. Ahamdi, M.; Harlen, O. G. *J. Comp. Phys.* **2008**, *227*, 7543-7560.

27. Phan-Thien, N.; Tanner, R. I. *J. Non-Newtonian Fluid Mech.* **1977**, *2*, 353-365.

483 28. Otsuki, Y.; Umeda, T.; Tsunori, R.; Shinohara, M. *Nihon Reoroji Gakkaishi* **2005**, *33*,
484 9-16.
485 29. Otsuki, Y.; Kajiwara, T.; Funatsu, K. *Polym. Eng. Sci.* **1999**, *39*, 1969-1981.
486 30. Matsunaga, K.; Kajiwara, T.; Funatsu, K. *Polym. Eng. Sci*. **1998**, *38*, 1099-1111.
487 31. Tackx, P.; Tacx, J. C. J. F. *Polymer* **1998**, *39*, 3109-3113.
488 32. Yamaguchi, M.; Takahashi, M. *Polymer* **2002**, *42*, 8663-8670.
489 33. Mieda, N.; Yamaguchi, M. *Adv. Polym. Technol.* **2007**, *26*, 173-181.
490 34. Levitt, L.; Macosko, C. W.; Pearson, S. D. *Polym. Eng. Sci*. **1996**, *36*, 1647-1655.
491 35. Goddard, J. D. *J. Non-Newtonian Fluid Mech.* **1976**, *2*, 1-17.
492 36. Pipes, R. B.; Hearle, J. W. S.; Beaussart, A. J.; Sastry, A. M.; Okine R. K. *Compos.*
493 *Mater.* **1991**, *25*, 1204-1217.
494 37. Carrara, A. S.; Mcgarry, F. J. *J. Comp. Mat*. **1968**, *2*, 222-243.
495 38. Harris, B., *Engineering Composite Materials*, 2nd ed. **1999**, Maney Publishing,
496 Leeds.
497 39. Goh, K. L.; Mathias, K. J.; Aspden, R. M.; Hukins, D. W. H. *J. Mater. Sci*. **2000**, *35*,
498 2493-2497.
499